

# UC San Diego

## UC San Diego Previously Published Works

### Title

From hidden order to antiferromagnetism: Electronic structure changes in Fe-doped URu<sub>2</sub>Si<sub>2</sub>

### Permalink

<https://escholarship.org/uc/item/2t1154cz>

### Journal

Proceedings of the National Academy of Sciences of the United States of America, 118(27)

### ISSN

0027-8424

### Authors

Frantzeskakis, Emmanouil  
Dai, Ji  
Bareille, Cédric  
et al.

### Publication Date

2021-07-06

### DOI

10.1073/pnas.2020750118

Peer reviewed

# From hidden order to antiferromagnetism: Electronic structure changes in Fe-doped URu<sub>2</sub>Si<sub>2</sub>

Emmanouil Frantzeskakis<sup>a,1</sup>, Ji Dai<sup>a,b</sup>, Cédric Bareille<sup>c</sup>, Tobias C. Rödel<sup>a,d</sup>, Monika Güttler<sup>a,e</sup>, Sheng Ran<sup>f,g</sup>, Noravee Kanchanavatee<sup>f,h</sup>, Kevin Huang<sup>f,i</sup>, Naveen Pouse<sup>f,j</sup>, Christian T. Wolowiec<sup>f</sup>, Emile D. L. Rienks<sup>k</sup>, Pascal Lejay<sup>l</sup>, Franck Fortuna<sup>a</sup>, M. Brian Maple<sup>f,1</sup>, and Andrés F. Santander-Syro<sup>a,1</sup>

<sup>a</sup>CNRS, Institut des Sciences Moléculaires d'Orsay, Université Paris-Saclay, 91405 Orsay, France; <sup>b</sup>Institute of Physics and Lausanne Centre for Ultrafast Science, École Polytechnique Fédérale de Lausanne, CH-1015 Lausanne, Switzerland; <sup>c</sup>Institute for Solid State Physics, University of Tokyo, Chiba 277-8581, Japan; <sup>d</sup>Synchrotron SOLEIL, L'Orme des Merisiers, 91192 Gif-sur-Yvette, France; <sup>e</sup>Institut für Festkörperphysik, Technische Universität Dresden, D-01062 Dresden, Germany; <sup>f</sup>Department of Physics, University of California San Diego, La Jolla, CA 92093; <sup>g</sup>Department of Physics, Washington University in St. Louis, St. Louis, MO 63130; <sup>h</sup>Department of Physics, Chulalongkorn University, Pathumwan 10330, Thailand; <sup>i</sup>Materials Science Division, Lawrence Livermore National Laboratory, Livermore, CA 94550; <sup>j</sup>Strategic Space Systems Division, Northrop Grumman, Redondo Beach, CA 90278; <sup>k</sup>Helmholtz-Zentrum Berlin für Materialien und Energie, Elektronenspeicherring BESSY II, 12489 Berlin, Germany; and <sup>l</sup>Institut Néel, CNRS and Université Grenoble Alpes, F-38042 Grenoble, France

Contributed by M. Brian Maple, May 27, 2021 (sent for review October 7, 2020; reviewed by Claude Monney and Peter M. Oppeneer)

In matter, any spontaneous symmetry breaking induces a phase transition characterized by an order parameter, such as the magnetization vector in ferromagnets, or a macroscopic many-electron wave function in superconductors. Phase transitions with unknown order parameter are rare but extremely appealing, as they may lead to novel physics. An emblematic and still unsolved example is the transition of the heavy fermion compound URu<sub>2</sub>Si<sub>2</sub> (URS) into the so-called hidden-order (HO) phase when the temperature drops below  $T_0 = 17.5$  K. Here, we show that the interaction between the heavy fermion and the conduction band states near the Fermi level has a key role in the emergence of the HO phase. Using angle-resolved photoemission spectroscopy, we find that while the Fermi surfaces of the HO and of a neighboring antiferromagnetic (AFM) phase of well-defined order parameter have the same topography, they differ in the size of some, but not all, of their electron pockets. Such a nonrigid change of the electronic structure indicates that a change in the interaction strength between states near the Fermi level is a crucial ingredient for the HO to AFM phase transition.

heavy fermions | hidden order | electronic structure | ARPES

The transition of URu<sub>2</sub>Si<sub>2</sub> from a high-temperature paramagnetic (PM) phase to the hidden-order (HO) phase below  $T_0$  is accompanied by anomalies in specific heat (1–3), electrical resistivity (1, 3), thermal expansion (4), and magnetic susceptibility (2, 3) that are all typical of magnetic ordering. However, the small associated antiferromagnetic (AFM) moment (5) is insufficient to explain the large entropy loss and was shown to be of extrinsic origin (6). Inelastic neutron scattering (INS) experiments revealed gapped magnetic excitations below  $T_0$  at commensurate and incommensurate wave vectors (7–9), while an instability and partial gapping of the Fermi surface was observed by angle-resolved photoemission spectroscopy (ARPES) (10–16) and scanning tunneling microscopy/spectroscopy (17, 18). More recently, high-resolution, low-temperature ARPES experiments imaged the Fermi surface reconstruction across the HO transition, unveiling the nesting vectors between Fermi sheets associated with the gapped magnetic excitations seen in INS experiments (14, 19) and quantitatively explaining, from the changes in Fermi surface size and quasiparticle mass, the large entropy loss in the HO phase (19). Nonetheless, the nature of the HO parameter is still hotly debated (20–23).

The HO phase is furthermore unstable above a temperature-dependent critical pressure of about 0.7 GPa at  $T = 0$ , at which it undergoes a first-order transition into a large moment AFM phase where the value of the magnetic moment per U atom exhibits a sharp increase, by a factor of 10 to 50 (6, 24–30). When the system crosses the HO → AFM phase boundary, the characteristic magnetic excitations of the HO phase are either

suppressed or modified (8, 31), while resistivity and specific heat measurements suggest that the partial gapping of the Fermi surface is enhanced (24, 27).

As the AFM phase has a well-defined order parameter, studying the evolution of the electronic structure across the HO/AFM transition would help develop an understanding of the HO state. So far, the experimental determination of the Fermi surface by Shubnikov de Haas (SdH) oscillations only showed minor changes across the HO → AFM phase boundary (32). Here, we take advantage of the HO/AFM transition induced by chemical pressure in URu<sub>2</sub>Si<sub>2</sub>, through the partial substitution of Ru with Fe (33–37), to directly probe its electronic structure in the AFM phase using ARPES. As we shall see, our results reveal that changes in the Ru  $4d$ – $U$   $5f$  hybridization across the HO/AFM phase boundary seem essential for a better understanding of the HO state.

## Results and Discussion

Fig. 1A shows the phase diagram of URu<sub>2–x</sub>Fe<sub>x</sub>Si<sub>2</sub> as a function of Fe concentration ( $x$ ) and of the associated chemical

### Significance

The transition of URu<sub>2</sub>Si<sub>2</sub> to an ordered state below 17.5 K has been a puzzle of condensed matter physics for over 30 y, earning it the soubriquet of the hidden-order (HO) state. Intriguingly, pressure or doping can transform the HO into an antiferromagnetic (AFM) state, of well-known symmetry. Here, by angle-resolved photoemission spectroscopy, the electronic structure of URu<sub>2</sub>Si<sub>2</sub> in the HO phase is directly compared with its AFM counterpart. This reveals topographically identical Fermi surfaces; however, they differ by the size of some of their pockets. The overall nonrigid change of the electronic structure across the AFM/HO phase boundary indicates that a change in the interaction strength between states near the Fermi level is essential to stabilize the HO state.

Author contributions: M.B.M. and A.F.S.-S. designed research; E.F., J.D., C.B., T.C.R., M.G., and F.F. performed ARPES measurements, under the supervision of A.F.S.-S.; E.D.L.R. provided support with ARPES instrumentation; S.R., N.K., K.H., N.P., C.T.W., P.L., and M.B.M. prepared and characterized single crystals; E.F., C.B., and A.F.S.-S. analyzed and interpreted data; E.F. and A.F.S.-S. wrote the paper. All authors discussed extensively the results and the manuscript.

Reviewers: C.M., University of Fribourg; and P.M.O., Uppsala University.

The authors declare no competing interest.

Published under the PNAS license.

<sup>1</sup>To whom correspondence may be addressed. Email: emmanouil.frantzeskakis@universite-paris-saclay.fr, mbmaple@ucsd.edu, or andres.santander-syro@universite-paris-saclay.fr.

This article contains supporting information online at <https://www.pnas.org/lookup/suppl/doi:10.1073/pnas.2020750118/-DCSupplemental>.

Published June 29, 2021.

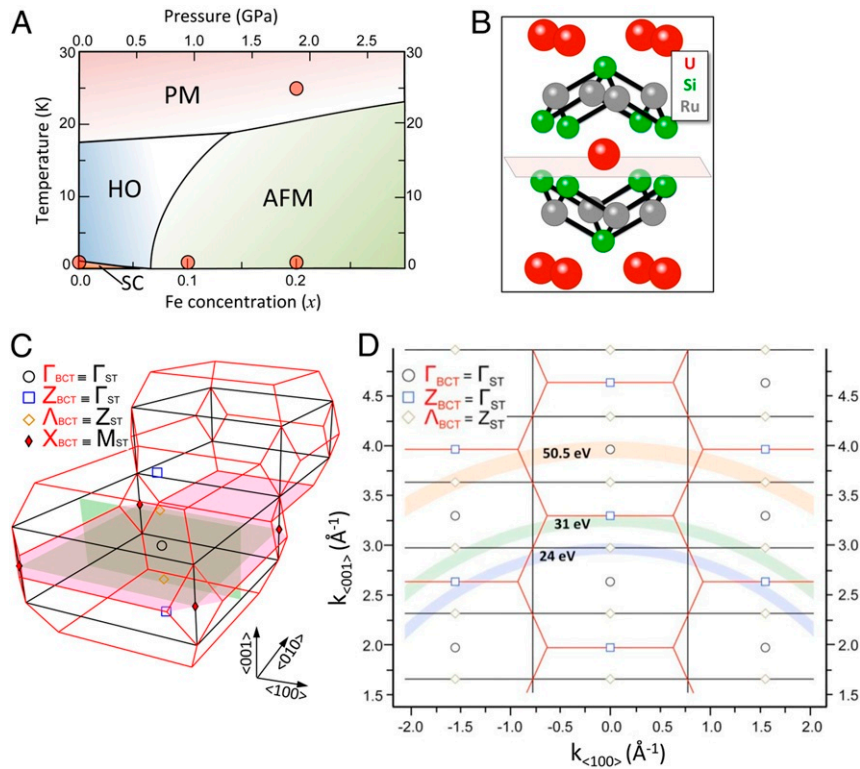


**Fig. 1.** (A) Temperature phase diagram of  $\text{URu}_{2-x}\text{Fe}_x\text{Si}_2$  as a function of Fe concentration and equivalent chemical pressure as determined by electrical resistivity, specific heat, magnetization, thermal expansion, and neutron diffraction measurements (33, 34, 36, 37). The markers denote the different compositions/temperatures studied in the present work. Henceforth, blue and green hues will be used to represent ARPES data in the HO and AFM states, respectively. SC, superconducting. (B) Schematic unit cell showing a natural Si-terminated cleavage plane. (C) Bulk BCT (red lines, PM phase) and ST (black lines, HO and AFM phases) Brillouin zones. The typical in-plane (red) and out-of-plane (green) measurement planes, together with the high-symmetry  $\Gamma$ , Z, and  $\Lambda$  points, are also shown. Note that, in the folded ST Brillouin zone, the  $\Gamma$  and Z points of the BCT zone become equivalent, and  $Z_{\text{ST}} = \Lambda_{\text{BCT}}$ . (D) Reciprocal  $k_{<100>} - k_{<001>}$  plane showing the spherical caps in  $k$  space probed with 50.5-, 31-, and 24-eV photons for different emission angles of the photoelectrons, within the free-electron model of the photoemission final states. Black (red) lines denote the borders of the ST (BCT) Brillouin zone. Damping of the final states results in broadening of the surface-perpendicular wave vector. The corresponding uncertainty ( $\delta k_{\perp}$ ), represented by the widths of the arcs, is related to the photoelectron escape depth ( $\lambda$ ) as  $\delta k_{\perp} = 1/\lambda$  (38). The inner potential has been set to 13 eV (10, 11, 15, 19).

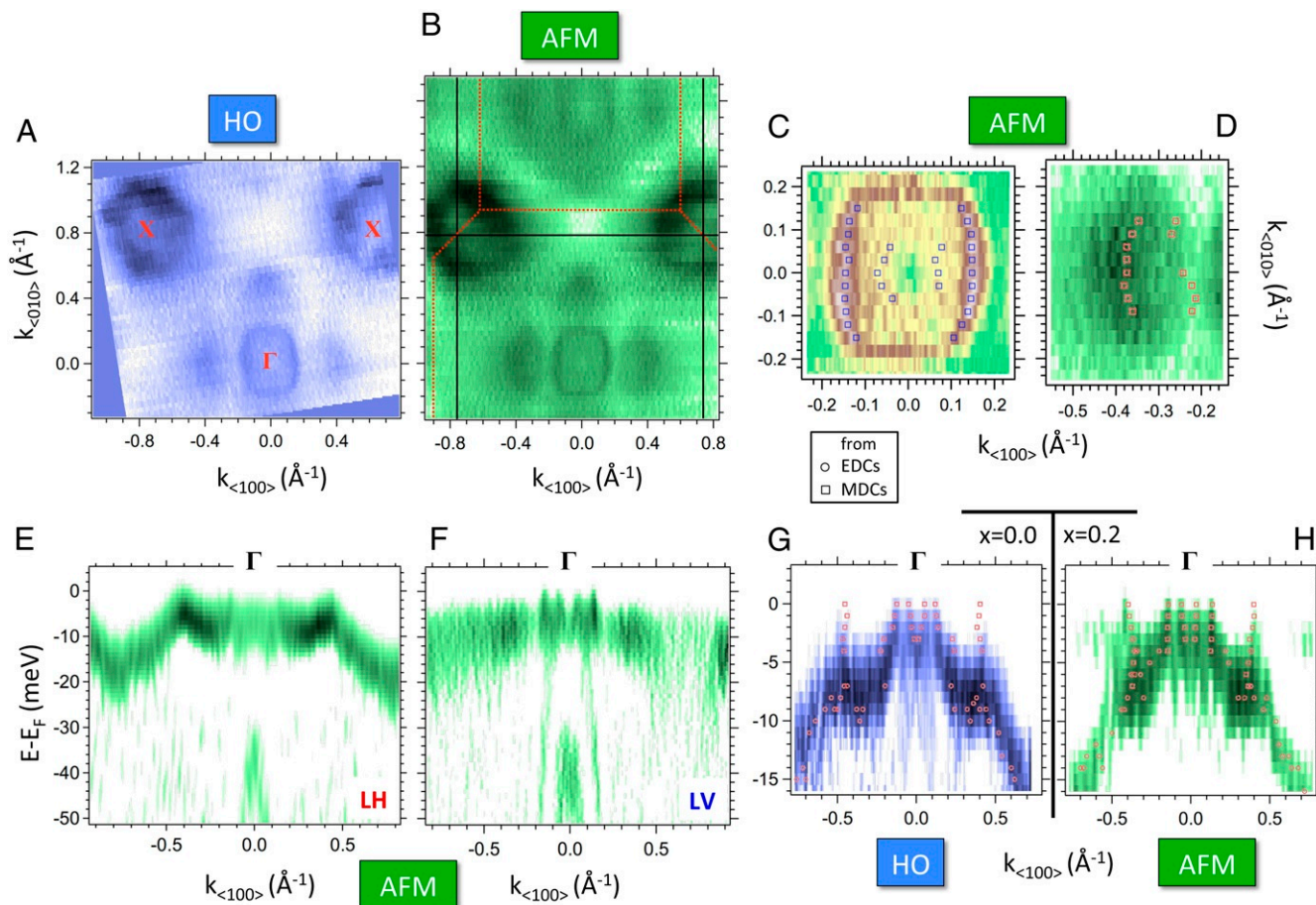
pressure. The quantum-critical transition at  $T = 0$  from the HO to the AFM phase occurs at  $x_c \approx 0.07$ . Our samples (orange markers) are characteristic of the HO, AFM, and PM phases. This study will focus on changes across the HO/AFM phase boundary. As schematized in Fig. 1B, henceforth we will characterize the electronic structure of Fe-doped  $\text{URu}_2\text{Si}_2$  (001) surfaces with an Si termination layer, which corresponds to a buried bulk-like U layer, as the bulk-derived heavy bands of U 5f origin are a key feature of the low-energy electronic structure of  $\text{URu}_2\text{Si}_2$  (11–13, 15, 16, 19). A detailed comparison with the alternative U-terminated surfaces and the stability of cleaved surfaces in ultrahigh vacuum are presented in *SI Appendix, sections SI.2 and SI.3*. Fig. 1C presents the three-dimensional (3D) body-centered tetragonal (BCT; PM phase, red lines) and simple-tetragonal (ST; HO and AFM phases, black lines) Brillouin zone of  $\text{URu}_2\text{Si}_2$  and highlights the typically measured planes. Fig. 1D illustrates how reciprocal space is probed using photon energies of 50.5, 31, and 24 eV. At normal emission ( $k_{<100>} = 0$ ), these energies correspond to bulk  $\Gamma$ , Z, and  $\Lambda$  high-symmetry points of the BCT Brillouin zone. In the neighboring Brillouin zones, the same photon energies probe the states near the  $\Lambda$  (50.5 and 31 eV) and Z (24 eV) high-symmetry points.

Fig. 2A and B shows the experimental in-plane Fermi surface of pure and Fe-doped  $\text{URu}_2\text{Si}_2$  in the low-temperature HO and AFM states, respectively. Their striking similarity demonstrates that the HO and AFM phases share common nesting vectors,

as inferred from INS experiments (7–9) and theoretical calculations (21, 40), and directly confirms conclusions from previous measurements of extremal Fermi surface contours by SdH oscillations, which showed only minor differences between the HO and the AFM phases (32).

Specifically, as seen from Fig. 2A and B, there are two Fermi sheets centered around  $\Gamma$ : an intense square-like outer contour with  $k_F \approx 0.15 \text{ \AA}^{-1}$  along  $k_{<100>}$  and a circumscribed weaker circular-like inner contour (Fig. 2C). These contours correspond, respectively, to hole-like and electron-like pockets. The pockets are formed by an M-shaped band resulting from the interaction between heavy and light states, as discussed in previous works on pure  $\text{URu}_2\text{Si}_2$  (19), and described by a phenomenological toy model in *SI Appendix, Figs. S7 and S8 and section SI.4*. At larger  $k_{<100>}$  momenta of the order of 0.3 to 0.4  $\text{ \AA}^{-1}$ , there are four off-centered “Fermi petals” symmetrically distributed around  $\Gamma$  (19), which are shown in detail in Fig. 2D. All these Fermi sheets around  $\Gamma$  agree well with previous local spin-density approximation calculations in the AFM phase of  $\text{URu}_2\text{Si}_2$  (21, 41). Additionally, large electron pockets centered at the corners of the ST Brillouin zone (the X points) are observed in both the HO and AFM states (Fig. 2A and B). These pockets arise from the interaction (hybridization) of heavy bands of U 5f character with a dispersing hole-like band (19).

Fig. 2E and F presents band dispersions of Fe-doped  $\text{URu}_2\text{Si}_2$  along  $k_{<100>}$  using photons with linear horizontal (LH) and linear vertical (LV) polarization, respectively. The dispersion of the



**Fig. 2.** (A and B) In-plane Fermi surface maps of pure (blue hues) and Fe-doped (green hues)  $\text{URu}_2\text{Si}_2$  in the HO and AFM phases, respectively. Red and black lines denote the BCT and ST Brillouin zones. (C and D) Zoomed-in views of two characteristic common features of the HO and AFM states, here measured on a  $\text{URu}_{1.9}\text{Fe}_{0.1}\text{Si}_2$  sample in the AFM state: the pockets around  $\Gamma$  and the off-centered Fermi petals, respectively. (E and F) Near- $E_F$  energy dispersion of Fe-doped  $\text{URu}_2\text{Si}_2$  using photons with LH or LV polarization as to enhance  $f$ - and  $d$ -derived features, respectively. (G and H) High-resolution ARPES energy-momentum dispersions around  $\Gamma$  along  $k_{<100>}$  in the HO phase of  $\text{URu}_2\text{Si}_2$  and the AFM phase of  $\text{URu}_{1.8}\text{Fe}_{0.2}\text{Si}_2$ , respectively. Photons with LH polarization were used. All data in this figure were measured at 1 K with 50.5-eV photons. In order to enhance the experimental features, the 2D curvature of the ARPES intensity is presented (39). The Fermi surface maps are a superposition of identical measurements using photons with LH and LV polarization, in order to display all of the features with different orbital character. Markers in C, D, G, and H show the local maxima of the spectral function extracted from either EDCs (circles) or momentum distribution curves (MDCs; squares).

heavy bands can be best detected using LH photons, while a light hole-like band and the M-shaped feature are best probed with LV photons. The necessity for light with variable polarization reflects the different orbital character of those states, namely the heavy bands of U  $5f$  origin and the light bands of likely Ru  $4d$  origin. The phenomenological model presented in *SI Appendix, section SI.4* includes two pairs of bands with very different effective masses to mimic the light and heavy bands. Finally, the hole-like band with a maximum at  $E - E_F \approx -30$  meV is common to both polarizations and corresponds to a surface state (42).

Fig. 2 G and H shows a zoomed-in view of the near- $E_F$  electronic dispersion around  $\Gamma$ , both for the pure and Fe-doped compounds. One clearly observes the M-shaped band around  $k_{<100>} = 0$  forming the outer square-like hole pocket and inner circular-like electron pocket. The shallow Fermi petals form above the “spikes” of the M-shaped band at  $k_{<100>} \approx 0.4 \text{ \AA}^{-1}$ . Our experimental resolution, which worsens as photon energy increases, does not allow us to draw conclusions about electronic structure changes around  $\Gamma$  between the pure (HO) and Fe-doped (AFM) compounds. On the other hand, as we shall see next, the electronic structure around the  $\Lambda$  and Z points,

which are both probed with smaller photon energies, shows clear changes between the two phases.

Fig. 3 compares the near- $E_F$  electronic structure of  $\text{URu}_{2-x}\text{Fe}_x\text{Si}_2$  in the HO ( $x=0$ ) and deep into the AFM ( $x=0.2$ ) (33–35, 37, 43) phases, around the Z and  $\Lambda$  high-symmetry points of the BCT Brillouin zone. We observe small but unequivocal changes around these points within the first few millielectronvolts below the Fermi level. In particular, both in the HO phase (Fig. 3 A–D) and in the AFM phase (Fig. 3 G–J), the band dispersions around Z and  $\Lambda$  exhibit a clear M-shaped feature with an electron pocket centered at  $k_{<100>} = 0$ . However, the band minimum of this electron pocket, located at  $E - E_F = (-5 \pm 0.5)$  meV in the HO state, is pushed up in energy to  $E - E_F = (-3 \pm 0.5)$  meV in the AFM state. This is also seen from the gray momentum-integrated energy distribution curves (EDCs) around Z and  $\Lambda$ , shown in Fig. 3 E, F, K, and L. More important, as demonstrated by the momentum-integrated magenta EDCs in Fig. 3 E, F, K, and L, such changes do not correspond to a rigid energy shift, as there are no observable differences in the binding energy of the heavy bands at large momenta ( $k_{<100>} = 0.3 \text{ \AA}^{-1}$ ), far from the hybridization region (around  $k_{<100>} = 0$ ). *SI Appendix, section SI.4* presents

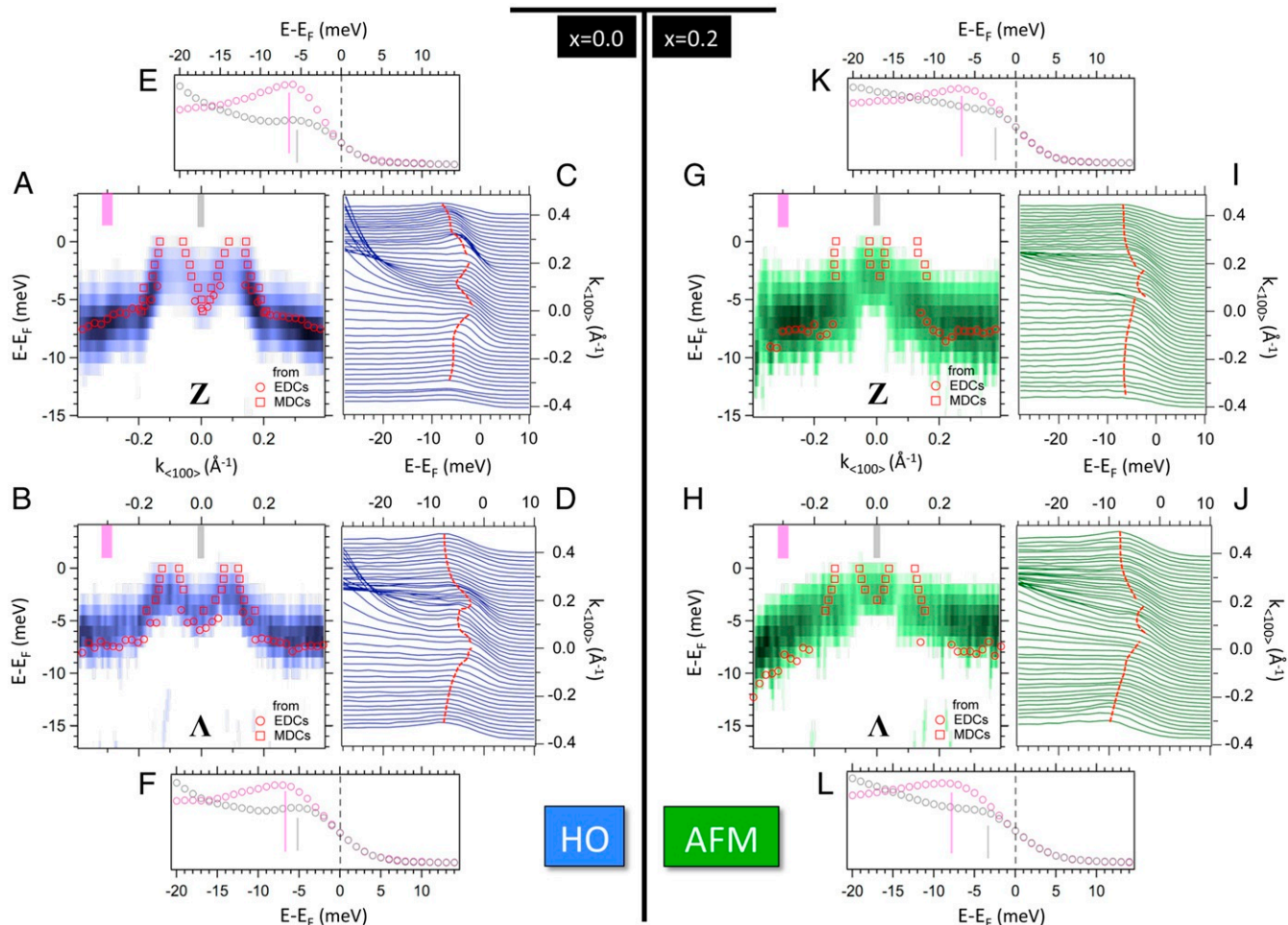


**Fig. 3.** (A and B) High-resolution ARPES energy-momentum maps [2D curvatures (39)] in the HO phase (pure  $\text{URu}_2\text{Si}_2$ ) around the Z and  $\Lambda$  points, respectively. Red markers show the local maxima of the spectral function extracted from either EDCs (circles) or momentum distribution curves (MDCs; squares). (C and D) Corresponding EDCs of the raw ARPES data. Dashed red lines are guides to the eye. (E and F) EDCs at  $k_{\langle 100 \rangle} = 0$  (gray circles) and  $k_{\langle 100 \rangle} = 0.3 \text{ \AA}^{-1}$  (magenta circles) around Z and  $\Lambda$ , respectively. Thin vertical lines mark the energy of the corresponding EDC peak. The EDCs were integrated over the momenta range shown by the thick bars in A and B. (G–L) Measurements analogous to A–F in the AFM phase ( $\text{URu}_{1.8}\text{Fe}_{0.2}\text{Si}_2$ ). To facilitate comparisons, energy-momentum maps in B and H have been interpolated in the energy direction before taking the curvature. The original energy step was 2 meV. Data around Z and  $\Lambda$  have been acquired using 31- and 24-eV photons with LH polarization, respectively. All data were measured at 1 K.

complementary analyses of the band structure changes between the HO and AFM phases around Z and  $\Lambda$ , as well as a comparison of the out-of-plane dispersions in both phases (SI Appendix, section SI.5), and a discussion of the changes in electronic structure at fixed doping ( $x = 0.2$ ) across the PM/AFM transition (SI Appendix, section SI.6). The latter is qualitatively the same as those observed across the PM/HO transition (19), namely the gapping of a large diamond-like Fermi surface around  $\Gamma$  along  $k_{\langle 110 \rangle}$  and the concomitant formation of the four Fermi petals, as discussed in Fig. 2.

The direct observation of a slight but distinct electronic band structure change across the HO/AFM phase boundary gives crucial insight to previous results obtained by other experimental probes. Specifically, extremal Fermi surface contours by SdH oscillations showed only minor differences between the HO and the AFM phases (32), while transport measurements concluded that the partially gapped Fermi surface of the HO phase (1) would be further gapped, and/or its volume reduced (decrease in the Sommerfeld coefficient), when the system is driven into the AFM phase (27, 33). Moreover, INS experiments suggested that the Fermi surface pockets at the  $\Gamma$ , Z, and/or  $\Sigma$  (connecting two Fermi petals) wave vectors should slightly distort upon crossing the HO/AFM phase boundary, so as to modify the opti-

mal energy for nesting (43). In agreement with those previous findings indicating only subtle Fermi surface changes that might be a consequence of better nesting conditions, our results in the AFM phase, compared with those in the HO phase, show a slightly modified electronic structure. Specifically, we observe an upward energy shift of the electron pockets around the Z and  $\Lambda$  high-symmetry points. Given the isotropic shape of the electron-like pocket around  $k = 0$  (Fig. 2C), an upward energy shift would be translated into a concomitant reduction of the corresponding Fermi surface contours, resulting in a smaller number of charge carriers in the AFM state. It is worth noting that, according to recent electronic structure calculations, a decrease in the volume of the unit cell, such as the one induced by chemical pressure through the partial substitution of Ru with Fe, would induce an energy shift in the opposite direction to the one experimentally observed at the Z and  $\Lambda$  points (41). We conclude that across the HO/AFM phase boundary, changes of the interaction strength between states near the Fermi level are at the origin of a minor but essential Fermi surface change in the system, stabilizing one or the other phase. We thus hope that our work will motivate further theoretical studies of the AFM phase of  $\text{URu}_2\text{Si}_2$  aiming to couple the observed energy shifts with the effect of the AFM nesting vectors (44).

As predicted by some models (45), pressure (physical or chemical) may have the effect of decreasing the Ru  $4d$ – $U$   $5f$  interaction strength to a critical value below which the conduction  $d$  carriers that were coupled to localized  $f$  electrons are no longer able to screen the magnetic interactions of the latter. Therefore, at high pressures, due to unscreened magnetic moments, the system is driven into the AFM phase.

More generally, within the Mott–Doniach picture of heavy fermion systems (46, 47), the competition between AFM interactions and the Kondo effect leads to a quantum phase transition between an AFM ground state, characterized by localized-like  $f$  electrons, and a Kondo lattice of itinerant  $f$  electrons. Our results show that the interaction strength of near- $E_F$  electronic states is another crucial ingredient that needs to be taken into account in the understanding of the phase diagram and quantum phase transitions of heavy fermion systems.

## Materials and Methods

**Crystal Growth and Characterization.** Single crystals of (Fe-doped)  $URu_2Si_2$  were grown in a tetraarc furnace using the Czochralski method in an argon atmosphere. The quality of the synthesized crystals was confirmed by X-ray diffraction measurements. Sample pieces were oriented by Laue diffraction. *SI Appendix, section SI.1* presents further details about the preparation and characterization of  $URu_{2-x}Fe_xSi_2$  single crystals.

**ARPES Measurements.** ARPES measurements were performed at the UE112-PGM-2b-1<sup>3</sup> end station of BESSY II with a Scienta R4000 hemispherical electron analyzer. Data for angle-resolved measurements were collected with photon energies between 20 and 67 eV. Higher photon energies were used for angle-integrated measurements (*SI Appendix, section SI.2*). The instrumental resolution varied from 3 to 7 meV according to experimental conditions. The light polarization was LH or LV as mentioned in the figures.

1. M. B. Maple *et al.*, Partially gapped Fermi surface in the heavy-electron superconductor  $URu_2Si_2$ . *Phys. Rev. Lett.* **56**, 185 (1986).
2. T. T. M. Palstra *et al.*, Superconducting and magnetic transitions in the heavy-fermion system  $URu_2Si_2$ . *Phys. Rev. Lett.* **55**, 2727 (1985).
3. W. Schlabitz *et al.*, Superconductivity and magnetic order in a strongly interacting Fermi-system:  $URu_2Si_2$ . *Z. Phys. B* **62**, 171 (1986).
4. A. de Visser *et al.*, Thermal expansion and specific heat of monocrystalline  $URu_2Si_2$ . *Phys. Rev. B* **34**, 8168(R) (1986).
5. C. Broholm *et al.*, Magnetic excitations and ordering in the heavy-electron superconductor  $URu_2Si_2$ . *Phys. Rev. Lett.* **58**, 1467 (1987).
6. K. Matsuda, Y. Kohori, T. Kohara, K. Kuwahara, H. Amitsuka, Spatially inhomogeneous development of antiferromagnetism in  $URu_2Si_2$ : Evidence from <sup>29</sup>Si NMR under pressure. *Phys. Rev. Lett.* **87**, 087203 (2001).
7. C. R. Wiebe *et al.*, Gapped itinerant spin excitations account for missing entropy in the hidden-order state of  $URu_2Si_2$ . *Nat. Phys.* **3**, 96 (2007).
8. A. Villaume *et al.*, Signature of hidden order in heavy fermion superconductor  $URu_2Si_2$ : Resonance at the wave vector  $Q_0 = (1, 0, 0)$ . *Phys. Rev. B* **78**, 012504 (2008).
9. N. P. Butch *et al.*, Symmetry and correlations underlying hidden order in  $URu_2Si_2$ . *Phys. Rev. B* **91**, 035128 (2015).
10. J. D. Denlinger *et al.*, Comparative study of the electronic structure of  $XRu_2Si_2$ : Probing the Anderson lattice. *J. Electron. Spectrosc. Relat. Phenom.* **117–118**, 347 (2001).
11. A. F. Santander-Syro *et al.*, Fermi-surface instability at the ‘hidden-order’ transition of  $URu_2Si_2$ . *Nat. Phys.* **5**, 637 (2009).
12. R. Yoshida *et al.*, Observation of the two fine structures related to the hidden order in the spectral functions of  $URu_2Si_2$ . *Phys. Rev. B* **85**, 241102(R) (2012).
13. R. Yoshida *et al.*, Translational symmetry breaking and gapping of heavy-quasiparticle pocket in  $URu_2Si_2$ . *Sci. Rep.* **3**, 2750 (2013).
14. J.-Q. Meng *et al.*, Imaging the three-dimensional fermi-surface pairing near the hidden-order transition in  $URu_2Si_2$  using angle-resolved photoemission spectroscopy. *Phys. Rev. Lett.* **111**, 127002 (2013).
15. F. L. Boariu *et al.*, Momentum-resolved evolution of the Kondo lattice into “hidden order” in  $URu_2Si_2$ . *Phys. Rev. Lett.* **110**, 156404 (2013).
16. S. Chatterjee *et al.*, Formation of the coherent heavy fermion liquid at the hidden order transition in  $URu_2Si_2$ . *Phys. Rev. Lett.* **110**, 186401 (2013).
17. A. R. Schmidt *et al.*, Imaging the Fano lattice to ‘hidden order’ transition in  $URu_2Si_2$ . *Nature* **465**, 570 (2010).
18. P. Aynajian *et al.*, Visualizing the formation of the Kondo lattice and the hidden order in  $URu_2Si_2$ . *Proc. Natl. Acad. Sci. U.S.A.* **107**, 10383 (2010).
19. C. Baille *et al.*, Momentum-resolved hidden-order gap reveals symmetry breaking and origin of entropy loss in  $URu_2Si_2$ . *Nat. Commun.* **5**, 4326 (2014).

The size of the beam spot was 40  $\mu\text{m}$ . Samples were cleaved in situ at a temperature below 20 K. The pressure was at all times lower than  $1.0 \times 10^{-10}$  mbar. The raw ARPES spectra were normalized to the total intensity of the EDCs and—if necessary—served to calculate the two-dimensional (2D) curvature (39). All data comparisons refer to identical experimental conditions and data treatment. The results have been reproduced in at least five different cleaves. The location of the normal-emission high-symmetry  $\Gamma$ ,  $\Lambda$ , and  $Z$  points was always double checked by performing in advance in-plane Fermi surface maps in steps of 0.5 or 0.25° around these points.

Similar to previous ARPES studies (15, 19), we note that although our low-temperature data (1 K) were acquired at slightly below the superconducting transition for  $x = 0$ , the corresponding energy gap (48) is at least one to two orders of magnitude smaller than our experimental resolution, and any possible changes associated with superconductivity cannot be seen in the present study.

**3D  $k$ -Space Mapping.** Within the free-electron final state model, ARPES measurements at constant photon energy give the electronic structure at the surface of a spherical cap of radius  $k = \sqrt{2m_e/\hbar^2} (h\nu - \Phi + V_0)^{1/2}$ . Here,  $m_e$  is the free-electron mass,  $\Phi$  is the work function, and  $V_0 = 13$  eV is the “inner potential” of  $URu_2Si_2$  (10, 11, 19, 42). Measurements around normal emission provide the electronic structure in a plane nearly parallel to the surface plane. Likewise, measurements as a function of photon energy provide the electronic structure in a plane perpendicular to the surface.

**Data Availability.** All study data are included in this article and *SI Appendix*.

**ACKNOWLEDGMENTS.** We thank Marie-Aude Méasson, Sergio G. Magalhães, and Peter Riseborough for comments and discussions. ARPES work at Institut des Sciences Moléculaires d’Orsay was supported by public grants from French National Research Agency (ANR) Project Fermi-Nest ANR-16-CE92-0018. Single-crystal growth at the University of California San Diego (UCSD) was supported by US Department of Energy, Office of Basic Energy Sciences, Division of Materials Sciences and Engineering Grant DE-FG02-04-ER46105. Sample characterization at UCSD was sponsored by NSF Grant DMR-1810310.

20. K. Haule, G. Kotliar, Arrested Kondo effect and hidden order in  $URu_2Si_2$ . *Nat. Phys.* **5**, 796 (2009).
21. S. Elgazzar, J. Ruzs, M. Amft, P. M. Oppeneer, J. A. Mydosh, Hidden order in  $URu_2Si_2$  originates from Fermi surface gapping induced by dynamic symmetry breaking. *Nat. Mater.* **8**, 337 (2009).
22. J. A. Mydosh, P. M. Oppeneer, Colloquium: Hidden order, superconductivity, and magnetism: The unsolved case of  $URu_2Si_2$ . *Rev. Mod. Phys.* **83**, 1301 (2011).
23. J. A. Mydosh, P. M. Oppeneer, Hidden order behaviour in  $URu_2Si_2$  (a critical review of the status of hidden order in 2014). *Philos. Mag.* **94**, 3642 (2014).
24. M. W. McElfresh *et al.*, Effect of pressure on competing electronic correlations in the heavy-electron system  $URu_2Si_2$ . *Phys. Rev. B* **35**, 43 (1987).
25. H. Amitsuka *et al.*, Effect of pressure on tiny antiferromagnetic moment in the heavy-electron compound  $URu_2Si_2$ . *Phys. Rev. Lett.* **83**, 5114 (1999).
26. G. Motoyama, T. Nishioka, N. K. Sato, Phase transition between hidden and antiferromagnetic order in  $URu_2Si_2$ . *Phys. Rev. Lett.* **90**, 166402 (2003).
27. J. R. Jeffries, N. P. Butch, B. T. Yukich, M. B. Maple, Competing ordered phases in  $URu_2Si_2$ : Hydrostatic pressure and rhenium substitution. *Phys. Rev. Lett.* **99**, 217207 (2007).
28. N. P. Butch *et al.*, Antiferromagnetic critical pressure in  $URu_2Si_2$  under hydrostatic conditions. *Phys. Rev. B* **82**, 060408(R) (2010).
29. F. Bourdarot *et al.*, Magnetic properties of  $URu_2Si_2$  under uniaxial stress by neutron scattering. *Phys. Rev. B* **84**, 184430 (2011).
30. W. Knafo *et al.*, Destabilization of hidden order in  $URu_2Si_2$  under magnetic field and pressure. *Nat. Phys.* **16**, 942–948 (2020).
31. T. J. Williams *et al.*, Gapped excitations in the high-pressure antiferromagnetic phase of  $URu_2Si_2$ . *Phys. Rev. B* **95**, 195171 (2017).
32. E. Hassinger *et al.*, Similarity of the Fermi surface in the hidden order state and in the antiferromagnetic state of  $URu_2Si_2$ . *Phys. Rev. Lett.* **105**, 216409 (2010).
33. N. Kanchanavatee *et al.*, Twofold enhancement of the hidden-order/large-moment antiferromagnetic phase boundary in the  $URu_{2-x}Fe_xSi_2$  system. *Phys. Rev. B* **84**, 245122 (2011).
34. P. Das *et al.*, Chemical pressure tuning of  $URu_2Si_2$  via isoelectronic substitution of Ru with Fe. *Phys. Rev. B* **91**, 085122 (2015).
35. N. P. Butch *et al.*, Distinct magnetic spectra in the hidden order and antiferromagnetic phases in  $URu_{2-x}Fe_xSi_2$ . *Phys. Rev. B* **94**, 201102(R) (2016).
36. H.-H. Kung *et al.*, Analogy between the “hidden order” and the orbital antiferromagnetism in  $URu_{2-x}Fe_xSi_2$ . *Phys. Rev. Lett.* **117**, 227601 (2016).
37. S. Ran *et al.*, Phase diagram and thermal expansion measurements on the system  $URu_{2-x}Fe_xSi_2$ . *Proc. Natl. Acad. Sci. U.S.A.* **113**, 13348 (2016).
38. V. N. Strocov, Intrinsic accuracy in 3-dimensional photoemission band mapping. *J. Electron. Spectrosc. Relat. Phenom.* **130**, 65 (2003).

39. P. Zhang *et al.*, A precise method for visualizing dispersive features in image plots. *Rev. Sci. Instrum.* **82**, 043712 (2011).
40. H. Ikeda *et al.*, Emergent rank-5 nematic order in URu<sub>2</sub>Si<sub>2</sub>. *Nat. Phys.* **8**, 528–533 (2012).
41. P. M. Oppeneer *et al.*, Electronic structure theory of the hidden-order material URu<sub>2</sub>Si<sub>2</sub>. *Phys. Rev. B* **82**, 205103 (2010).
42. F. L. Boariu *et al.*, The surface state of URu<sub>2</sub>Si<sub>2</sub>. *J. Electron. Spectrosc. Relat. Phenom.* **181**, 82 (2010).
43. T. J. Williams, A. A. Aczel, M. B. Stone, M. N. Wilson, G. M. Luke, Hidden order signatures in the antiferromagnetic phase of U(Ru<sub>1-x</sub>Fe<sub>x</sub>)<sub>2</sub>Si<sub>2</sub>. *Phys. Rev. B* **95**, 104440 (2017).
44. P. M. Oppeneer *et al.*, Spin and orbital hybridization at specifically nested Fermi surfaces in URuSi<sub>2</sub>. *Phys. Rev. B* **84**, 241102 (2011).
45. Y. Dubi, A. V. Balatsky, Hybridization wave as the “hidden order” in URu<sub>2</sub>Si<sub>2</sub>. *Phys. Rev. Lett.* **106**, 086401 (2011).
46. N. F. Mott, Rare-earth compounds with mixed valencies. *Phil. Mag.* **30**, 403 (1974).
47. S. Doniach, The Kondo lattice and weak antiferromagnetism. *Phys. B+C* **91**, 231–234 (1977).
48. K. Hasselbach, J. R. Kirtley, P. Lejay, Point-contact spectroscopy of superconducting URu<sub>2</sub>Si<sub>2</sub>. *Phys. Rev. B* **46**, 5826 (1999).